(Received 10 April 2025, Accepted 14 May 2025, Scheduled 22 May 2025)

High-Gain Dual-Band Metasurface MIMO Antenna for Enhanced 5G and Satellite Applications

Hanbo Feng[1], Zhonggen Wang[1,*], Wenyan Nie[2], and Ming Yang[3]

[1] *School of Electrical and Information Engineering, Anhui University of Science and Technology, Huainan 232001, China*
[2] *School of Mechanical and Electrical Engineering, Huainan Normal University, Huainan 232001, China*
[3] *School of Electrical and communications Engineering, West Anhui University, Lu'an 237012, China*

ABSTRACT: In this paper, a novel single-layer dual-band metasurface MIMO antenna suitable for high-density 5G base stations, satellite terminals, and IoT devices is proposed. The antenna utilizes Characteristic Mode Analysis (CMA) to optimize the patch dimensions, achieving independent design for the low- and high-frequency bands. It also suppresses surface waves through a ground triple-slot structure. Additionally, the antenna abandons the traditional coplanar waveguide (CPW) and innovatively adopts an H-shaped slot feeding structure. This groundbreaking design successfully eliminates the need for complex matching networks and multi-layer stacking structures. Simulation and measurement results show that the MIMO antenna achieves an isolation below −22 dB and envelope correlation coefficient (ECC) less than 0.0025 in two operating frequency bands (4.13–5.94 GHz with a relative bandwidth of 36%; 7.68.4 GHz with a relative bandwidth of 10%), with a peak gain of 10.75 dB. Additionally, the antenna exhibits a diversity gain (DG) greater than 9.9 dB, with aperture efficiencies of 72% (low-frequency) and 36.8% (high-frequency). Compared with existing designs, the MIMO antenna proposed in this paper shows significant improvements in isolation, bandwidth flexibility, and structural simplicity.

1. INTRODUCTION

The rapid proliferation of 5G networks, satellite communications, and internet of things (IoT) ecosystems has intensified the demand for compact, multi-functional antennas capable of operating across diverse frequency bands while maintaining high isolation in densely packed multi-antenna systems. Dual-band antennas, in particular, are critical for supporting concurrent services such as sub-6 GHz 5G (45 GHz) and satellite downlinks (78 GHz), yet their design faces inherent trade-offs among bandwidth, isolation, and structural simplicity [1]. Conventional approaches, including U-slot microstrip patches [2] and defected ground structures (DGS) [3], often achieve dual-band operation at the cost of complex decoupling mechanisms. For instance, metal vias [4] and electromagnetic band-gap (EBG) layers [5] have been widely adopted to suppress surface waves, but these methods introduce multilayer fabrication processes or occupy significant lateral space, limiting their suitability for ultra-compact multiple-input multiple-output (MIMO) arrays [6]. Moreover, existing metasurface-integrated designs [7, 8], while enabling frequency agility, struggle to simultaneously address dual-band isolation and structural miniaturization, particularly in edge-to-edge configurations with sub-wavelength spacing.

As an electromagnetic field analysis method based on eigenvalue solution, CMA provides a systematic framework for mode manipulation in antenna design. Unlike traditional empirical parameter optimization, CMA can intuitively quantify the contribution of each mode to radiation (Mode Significance) and identify the impact of key geometric parameters on resonant frequencies and bandwidth, significantly enhancing design efficiency and interpretability [9–15]. In this paper, CMA is introduced into the optimization process of a dual-band metasurface antenna by analyzing the mode current distribution of an initial 4×4 square patch array, and it is clarified that the low-frequency band (4.13–5.94 GHz) is dominated by the fundamental mode (Mode 1) and the first-order mode (Mode 2), while the high-frequency band (7.6–8.4 GHz) is achieved by exciting a higher-order mode (Mode 17) through adjustments to the size of the corner patches, enabling independent design across both frequency bands. This approach avoids the blindness of traditional iterative trial-and-error methods and lays the theoretical foundation for mode decoupling and bandwidth expansion in ultra-compact dual-band MIMO antennas.

A key challenge lies in reconciling the conflicting requirements of wideband impedance matching, dual-band control, and ultra-low mutual coupling. Traditional feeding structures, such as CPW feeds, often necessitate intricate impedance transformers or parasitic elements to achieve multi-resonance behavior [16], complicating single-layer integration. Meanwhile, decoupling techniques relying on resonant metamaterials [17] or absorber layers [18] may degrade radiation efficiency or impose narrowband limitations. Recent advancements in slot-fed antennas [19] and metasurface superstrates [20] have shown promise in decoupling through radiation pattern diversification, yet their applicability to wideband dual-band systems remains underexplored. Moreover, many existing metasurface antennas [21–25] primarily focus on single-band, triple-band, or bandwidth extension designs, and also have not addressed

* Corresponding author: Zhonggen Wang (zgwang@ahu.edu.cn).

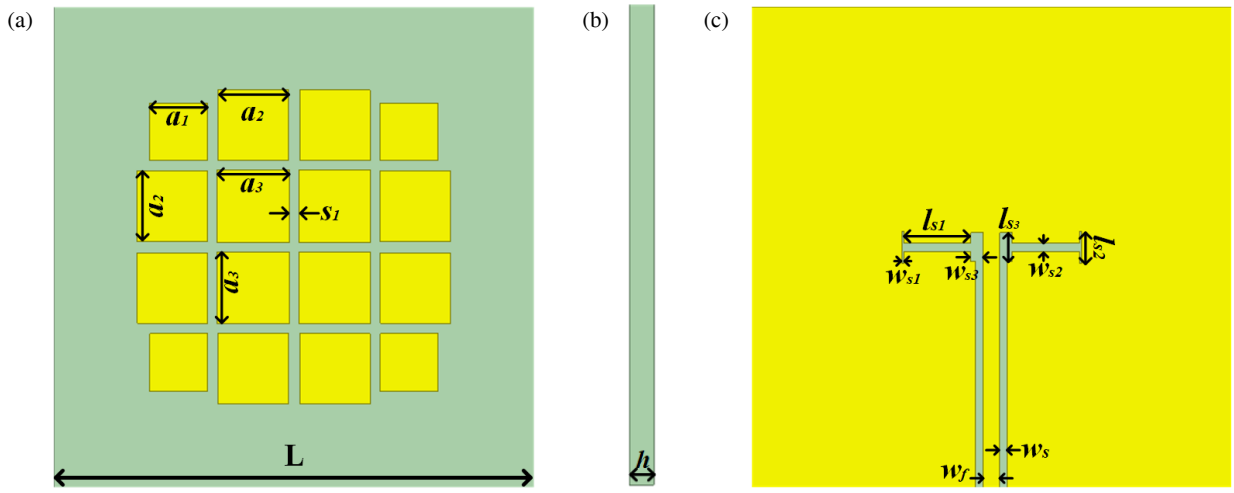

FIGURE 1. Configuration of the dual-band metasurface-based antenna. (a) Top view: $l = 60\,\text{mm}$, $a_1 = 7.2\,\text{mm}$, $a_2 = 8.8\,\text{mm}$, $a_3 = 9\,\text{mm}$, $s_1 = 0.6\,\text{mm}$ (b) Side view: $h = 3\,\text{mm}$ (c) Bottom view: $w_f = 2\,\text{mm}$, $w_s = 1\,\text{mm}$, $w_{s1} = 0.2\,\text{mm}$, $w_{s2} = 1\,\text{mm}$, $w_{s3} = 1.6\,\text{mm}$, $l_{s1} = 8.4\,\text{mm}$, $l_{s2} = 4\,\text{mm}$, $l_{s3} = 3.6\,\text{mm}$.

the collaborative design and isolation optimization of dual-band MIMO antennas. In this study, a novel dual-band metasurface-MIMO antenna is proposed innovatively, which employs an H-shaped slot feeding structure to replace the traditional CPW structure, achieving robust impedance matching across dual bands without the need for additional matching networks or multilayer stacking. This single-layer topology significantly reduces manufacturing complexity and cost, making it highly suitable for high-density deployment [26]. Meanwhile, three uniformly spaced slots etched on the antenna's ground plane are used to replace metal vias, disrupting surface wave propagation and achieving mutual coupling below $-22\,\text{dB}$ in both frequency bands. This planar decoupling strategy eliminates vertical interconnects, preserves the structural integrity of the antenna, and simplifies the manufacturing process [27]. The dual-band of the antenna can be designed independently. After the low-frequency band is determined, CMA is utilized to design and achieve the high-frequency bandwidth without affecting the low-frequency band. This design ensures flexibility in frequency tuning and eliminates cross-interference, representing a significant advancement compared with traditional coupled resonator architectures [16]. Compared to existing decoupling methods [3, 17], the proposed slitted ground plane minimizes fabrication complexity and avoids multilayer stacking. The design is validated through a 2×1 edge-to-edge array prototype, demonstrating robust performance in dual-band MIMO scenarios. This approach bridges the gap among high isolation, dual-band flexibility, and structural simplicity, addressing critical needs for next-generation wireless systems.

2. DUAL-BAND ANTENNA DESIGN AND ANALYSIS

2.1. Dual-Band Antenna Evolution and Performance

The structure of the proposed metasurface-based dual-band antenna is illustrated in Fig. 1. The antenna consists of a single-layer substrate with a 4×4 array of square patches on the top surface and a CPW feeding structure on the bottom side. The dielectric substrate is FR-4 ($\varepsilon_r = 4.4$, $\tan\delta = 0.003$) with a thickness of $h = 3\,\text{mm}$. The topology was designed using the Computer Simulation Technology (CST) software.

The design process comprises three steps. In Step 1, a conventional broadband metasurface slot antenna is proposed, which consists of a slot-feed structure and regular metal patches, as illustrated in Fig. 2(a). In Step 2, the antenna structure is simplified by directly integrating the feeding structure onto the ground plane, eliminating the need for a separate microstrip feedline and reducing the antenna structure to a single layer, as shown in Fig. 2(b). Subsequent results have verified that this simplification process may have an impact on high frequencies, but it does not affect the existing available frequency bands. This design not only simplifies the manufacturing process but also reduces costs. In Step 3, CMA is employed to analyze and optimize the patch size to achieve high-frequency bandwidth, while ensuring good impedance matching in the low-frequency band.

The $|S_{11}|$ and gains of the three antennas are shown in Fig. 3. As depicted in Fig. 3(a), Ant. 1 has a frequency band with $|S_{11}| < -10\,\text{dB}$ spanning from 4.29 to 5.51 GHz, with two resonances occurring at 4.56 GHz and 5.36 GHz, respectively. For Ant. 2, the frequency range where $|S_{11}| < -10\,\text{dB}$ is 4.2–5.78 GHz. For Ant. pro, the frequency range where $|S_{11}| < -10\,\text{dB}$ extends from 4.14 to 5.93 GHz and also from 7.6 to 8.4 GHz. There are two resonances at the low-frequency band, specifically at 4.42 GHz and 5.66 GHz, and another two resonances at the high-frequency band, occurring at 7.86 GHz and 8.24 GHz. As can be seen from Fig. 3(b), the peak gains of Ant. pro in the two frequency bands are 9.56 dB and 10.75 dB, respectively.

The 3D gain radiation patterns of the low-frequency resonant points during the antenna evolution process are shown in Fig. 4. The two resonant points of Ant. 1 in the low-frequency band exhibit a relatively uniform radiation pattern, with radiation pri-

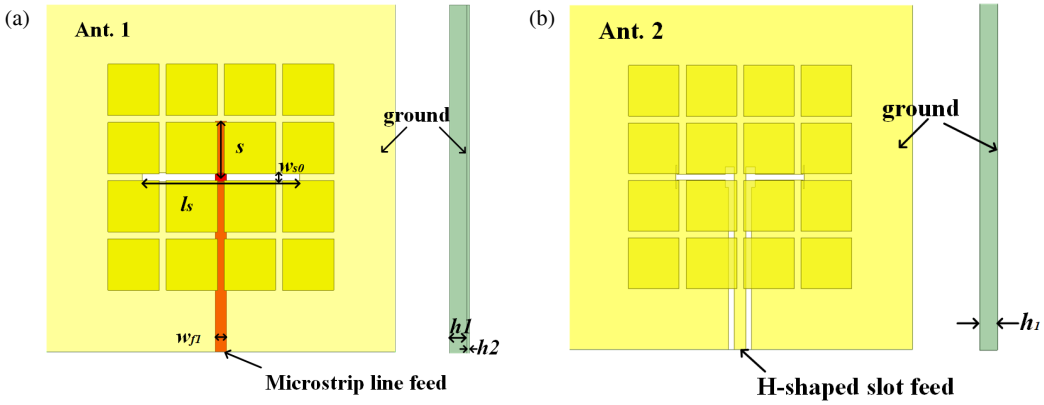

FIGURE 2. Antenna design. (a) Ant. step 1: $l_s = 27\,\text{mm}$, $s = 9\,\text{mm}$, $w_{s0} = 1.6\,\text{mm}$, $w_{f1} = 2\,\text{mm}$, $h_1 = 3\,\text{mm}$, $h_2 = 0.5\,\text{mm}$ (b) Ant. step 2: parameters are shown in Fig. 1(c).

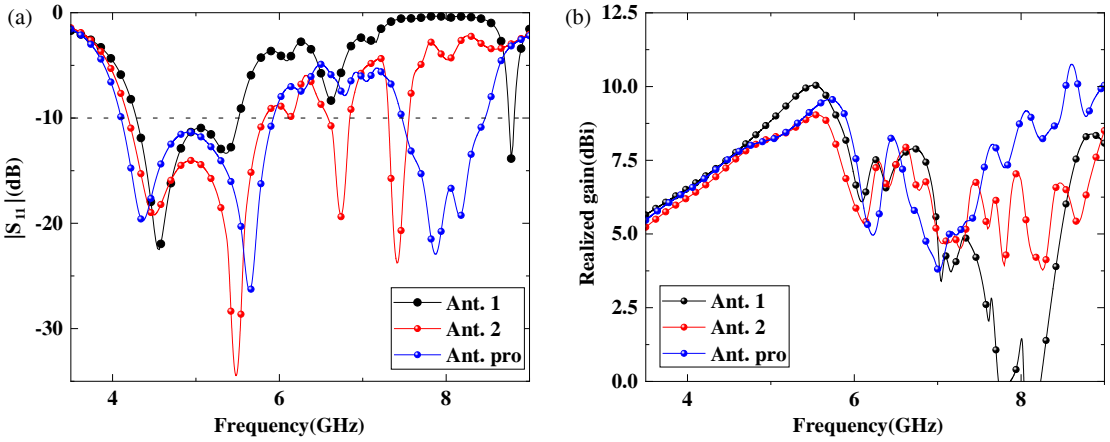

FIGURE 3. Performance of the three antennas. (a) S-parameters. (b) Realized gain.

marily propagating in one direction. For Ant. 2 and Ant. pro, although some multi-lobe characteristics appear at the second resonant point, they are not prominent, and the low-frequency band still exhibits a relatively uniform radiation pattern. From the figure, it can be seen that the simplification of the antenna structure and the evolution of the high-frequency band do not affect the initial low-frequency bandwidth.

2.2. Characteristic Mode Analysis

To illustrate the evolution process of the patch size, a detailed introduction will be provided through the characteristic mode analysis process. The initial antenna model is the most basic metasurface 4×4 square patch array antenna. By conducting characteristic mode simulations on the initial antenna model, we obtain the mode significance (MS) of the initial patch, as shown in Fig. 5. In this antenna design, three modes are utilized, namely Mode 1, Mode 2, and Mode 17, and their surface currents are depicted in Fig. 6.

Observing the surface currents of the three modes, it can be seen that Mode 1 and Mode 2 can be already excited in the basic array antenna model, working together with the slot-fed structure to achieve the available low-frequency bandwidth. However, Mode 17 cannot be excited as its surface current is concentrated around the perimeter, making it ineffective for coupling with the feeding structure. At the same time, we found that the surface currents of Mode 1 and Mode 2 were concentrated in the center, and the patches at the four corners have little influence on the coupling effect. Therefore, without affecting the low-frequency bandwidth, we attempted to reduce the size of the patches at the four corners to concentrate the current towards the center patches, enabling Mode 17 to be excited and achieving the available high-frequency bandwidth. In the meantime, slightly increase the central patch size to concentrate the current, which can effectively enhance the coupling area. After reducing the size of the patches at the four corners, the CMA was conducted again on the antenna model, and the resulting MS and surface currents are shown in Fig. 7 and Fig. 8(a). Observing the MS and surface currents, we found that the bandwidth in which Mode 17 can be excited has increased, and the current is also concentrated towards the center patches, as expected. As shown in Fig. 8(b), Mode 1 and Mode 2 exhibit single main-lobe radiation characteristics primarily oriented along the positive Z-axis direction in the 3D radiation patterns, respectively dominating the broadband coverage and directivity optimization in the low-frequency band. Meanwhile, Mode 17 excites a high-order multi-lobe structure, effectively supporting

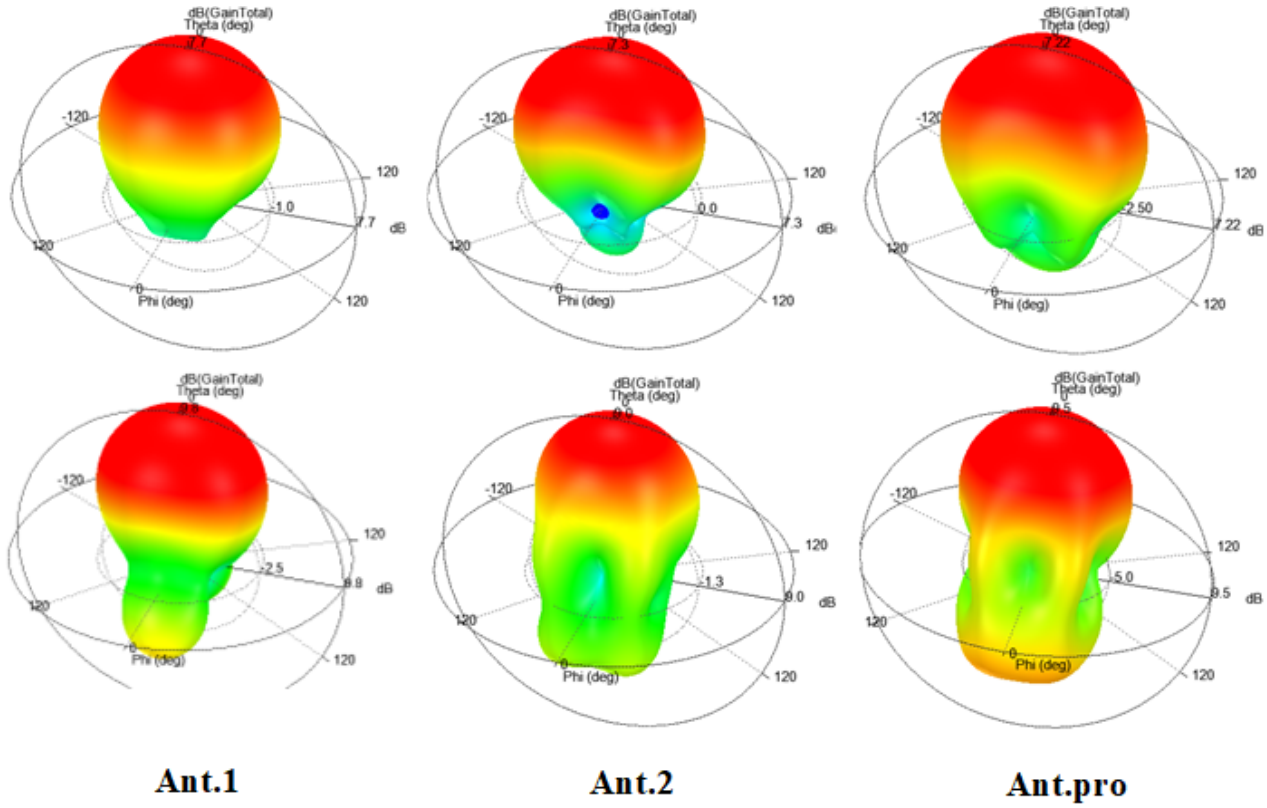

FIGURE 4. 3D gain radiation patterns at design stages.

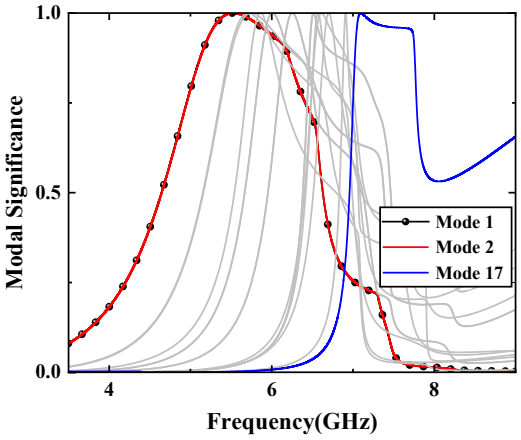

FIGURE 5. MS of the antenna.

multi-beam communication in the high-frequency band without compromising the overall antenna performance.

The feasibility of the scheme was verified through characteristic mode analysis, followed by a parametric analysis of the size of the four-corner patch. The results are shown in Fig. 9. Reducing the patch size to 7.2 mm achieved a high-frequency usable bandwidth.

2.3. Current Distribution

To gain a more intuitive understanding of the operating principles of the radio frequency components, we observe the surface current distribution of the antenna model as depicted in Fig. 10. At the resonant frequency of 4.42 GHz, the primary current forms a clear standing wave along the edge of the radiator, with a path length (18 mm) approximately one-quarter of the free-space wavelength ($\lambda_o = 67.8$ mm). This indicates that the antenna is based on a quarter-wavelength short-circuited resonance. Simultaneously, the H-shaped structure couples and excites secondary currents, whose path lengths match higher-order modes. The superposition effect of primary and secondary currents broadens the antenna's operational bandwidth through multi-mode resonance, providing the physical foundation for covering the 5G Sub-6 GHz frequency band. In contrast, at the resonant frequency of 5.64 GHz, the primary current forms a prominent standing wave distribution along the center of the radiator, with a path length (13.5 mm) precisely matching one-quarter of the free-space wavelength ($\lambda_o = 53.2$ mm) at this frequency point. Observing the current distribution at the two resonant frequencies within the high-frequency band, the primary currents are regularly arranged along the center of the radiator. The length of the current path (9 mm) is approximately one-quarter of the free-space wavelength at these two resonant points, indicating that the antenna operates in a 1/4-wavelength resonant mode at these resonant frequencies.

2.4. MIMO Antenna Design and Analysis

The configuration of the 2×1 antenna array is shown in Fig. 11. The two antenna elements based on the dual-frequency metasurface antenna presented in Fig. 1 remain unchanged, ex-

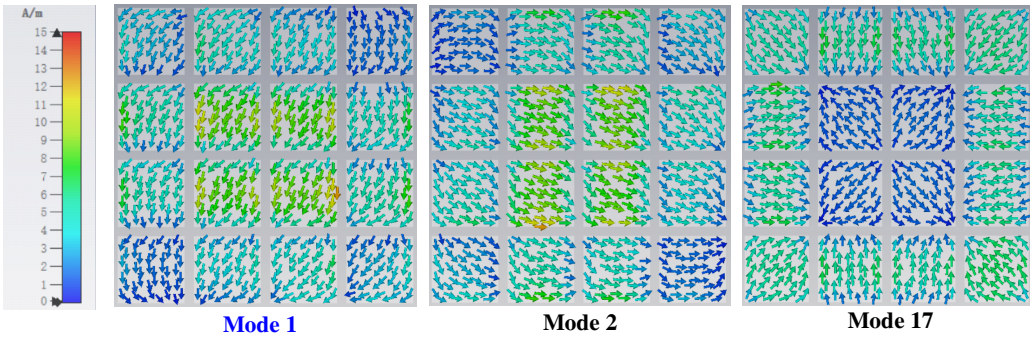

FIGURE 6. Modal currents of antenna.

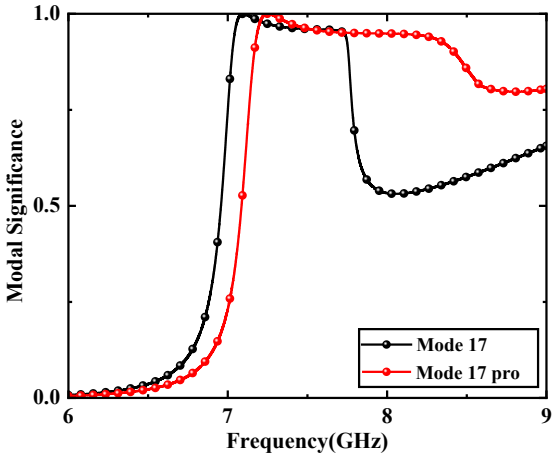

FIGURE 7. Comparison of MS results before and after patch size reduction.

cept that the overall dimensions are optimized to $lx \times ly = 100\,\text{mm} \times 60\,\text{mm}$ to ensure the operating frequency bands. Fig. 11(b) illustrates the configuration of the backplane for the 2×1 antenna array. In the central area of the antenna's ground plane, three slots are uniformly distributed and aligned parallel to the array's arrangement direction. Each slot has a width of 2 millimeters and a length of 50 millimeters, with a spacing of 2 millimeters between the slots. These slots fully penetrate the ground plane but do not extend through the dielectric substrate, thus maintaining the single-layer integrity of the structure. The antenna's feeding structure has been modified from the traditional CPW to an H-shaped slot feed. The arrangement of the backplane slots avoids the radiation area of the H-shaped slot to prevent interference with the feeding efficiency.

As shown in Fig. 12, a comparison of the currents before and after adding the isolation structure is presented. Without the isolation structure, the current forms a direct path between the two antennas, leading to the mutual coupling of electromagnetic energy. This cross-current can cause signal crosstalk and reduce isolation. After incorporating the isolation structure, the cross-flow path of the current is physically or electromagnetically blocked, and the current is primarily confined within the effective radiation area of each antenna, thereby significantly reducing the coupling effect.

The comparison of $|S_{21}|$ before and after slotting is shown in Fig. 13. Before slotting, $|S_{21}|$ was less than -14.4 dB. After introducing backplane slots, the high-frequency isolation is significantly enhanced, with $|S_{21}|$ remaining below -22 dB across the entire frequency band.

3. RESULTS AND DISCUSSION.

3.1. Measurement and Simulation

S-parameters were measured using a vector network analyzer, while the radiation pattern and gain were tested through standard gain horn antennas in an anechoic chamber, as shown in Figs. 14(a) and (b). Figs. 15(a) and (b) present the S-parameters and isolation of the antenna array from both measurements and simulations, which show good agreement with the simulated results.

Figure 16 shows the measured and simulated radiation patterns of the E-plane and H-plane at the center frequency of the low band and high band, respectively. The measured radiation pattern is in high agreement with the simulation results in terms of beam pointing, HPBW (Half Power Beam Width), and sidelobe level, with an error of less than 5%. The E-plane pattern exhibits significant unidirectional radiation, while the H-plane pattern approaches omnidirectional radiation. As shown in Figs. 16(c) and (d), the radiation pattern exhibits a "multi-lobe" characteristic, which is caused by the use of a higher-order mode (Mode 17) to achieve frequency band coverage. This higher-order mode causes multiple beams to radiate, leading to some distortion in the radiation pattern and a deviation from the original omnidirectional pattern, though the low-frequency band remains unaffected. However, this phenomenon does not negatively affect the overall performance of the antenna.

3.2. Envelope Correlation Coefficient

ECC is a metric that measures the degree of correlation between communication channels. In wireless communication systems, especially MIMO systems, ECC is used to quantify the correlation between antenna element channels. A lower ECC value indicates less correlation between antennas, which leads to better performance of the MIMO system [28]. As illustrated in Fig. 17, the ECCs within the two operating bands are below 0.0009 and 0.002, respectively, demonstrating excellent multiple-input multiple-output performance. When the ECC of the antenna approaches zero, the diversity gain (DG)

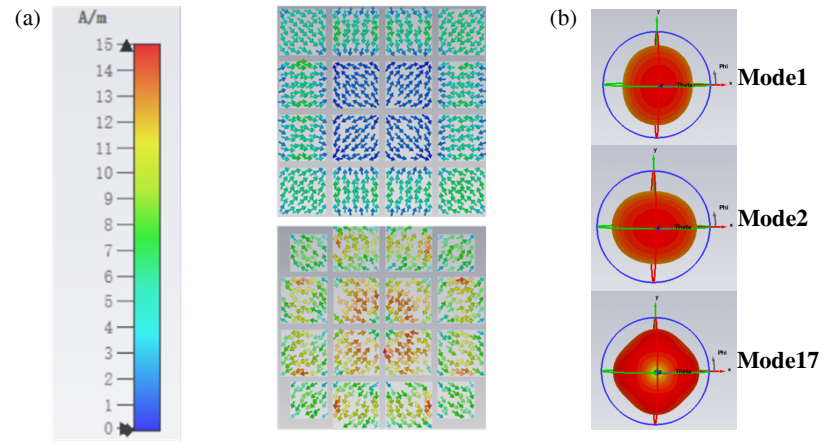

FIGURE 8. (a) Comparison of surface currents results before and after patch size reduction. (b) Modal radiation patterns of the three modes.

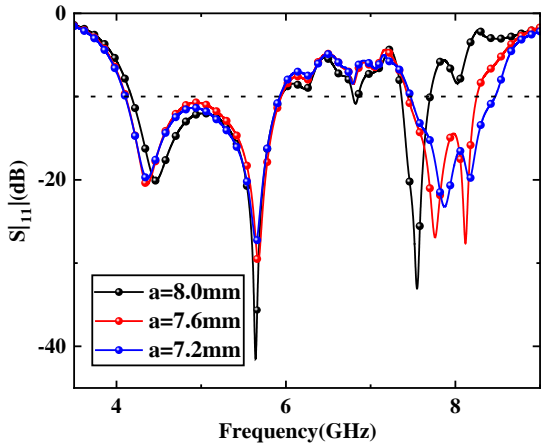

FIGURE 9. Comparison of S-parameters before and after optimization.

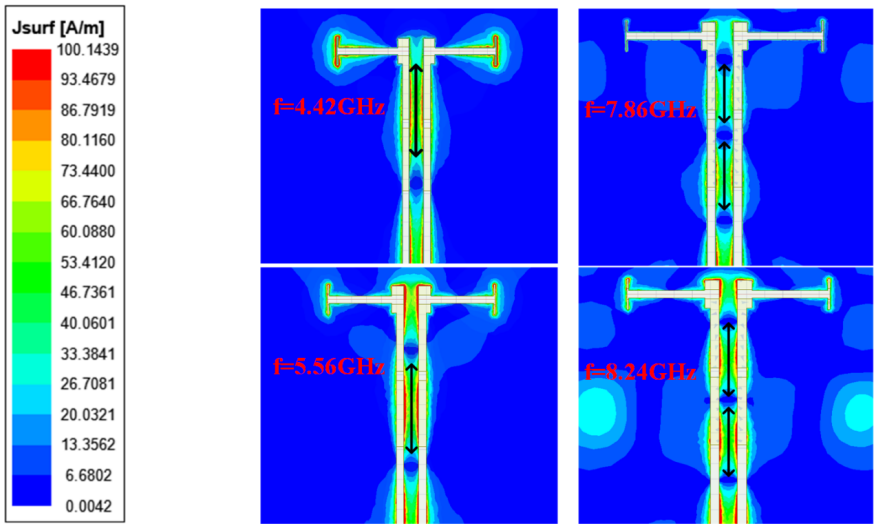

FIGURE 10. Surface current distribution of the antenna.

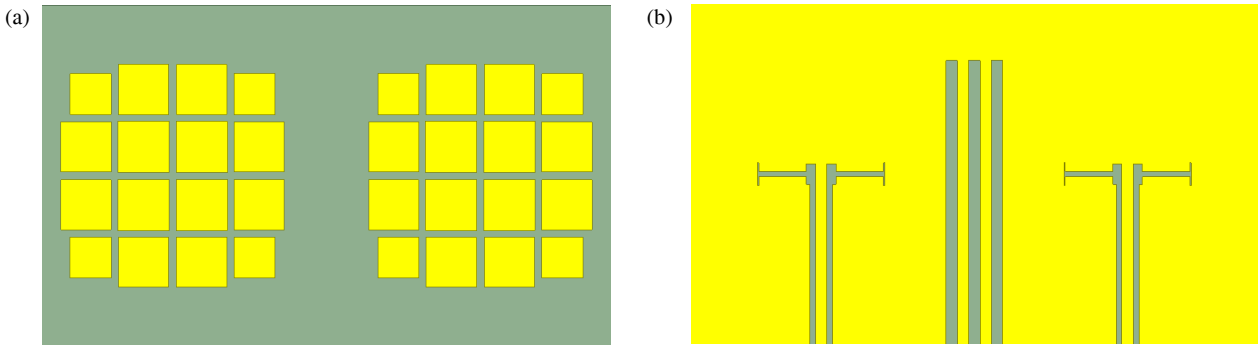

FIGURE 11. 2×1 antenna array. (a): Top view (b): Bottom view.

approaches the ideal value (DG $>$ 9.9 dB). The ECC can be calculated by using the following formula:

$$\rho_{ij} = \frac{\left|\iint_{4\pi} \bar{F}_i(\theta,\emptyset)\cdot\bar{F}_j^*(\theta,\emptyset)\,d\Omega\right|^2}{\iint_{4\pi}\left|\bar{F}_i(\theta,\emptyset)\right|^2 d\Omega\cdot\iint_{4\pi}\left|\bar{F}_j(\theta,\emptyset)\right|^2 d\Omega} \quad (1)$$

3.3. Antenna Performance Comparison

The proposed antenna demonstrates outstanding performance in dual-band design, with its gain (10.75 dB) being significantly higher than other dual-band antennas (e.g., 9.1 dB for [30] and 8.6 dB for [35]), and even surpassing some

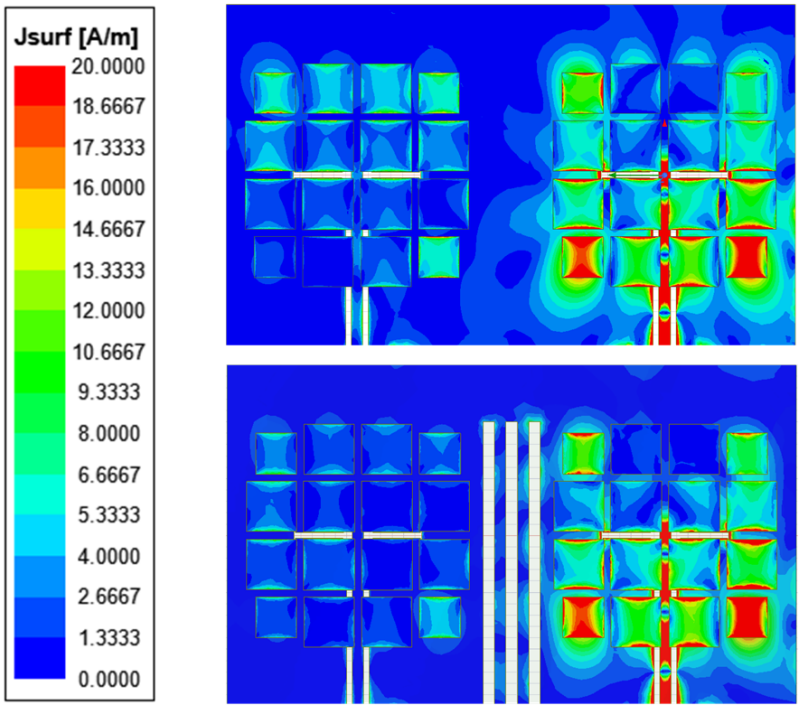

FIGURE 12. Comparison of current with and without the isolation structure.

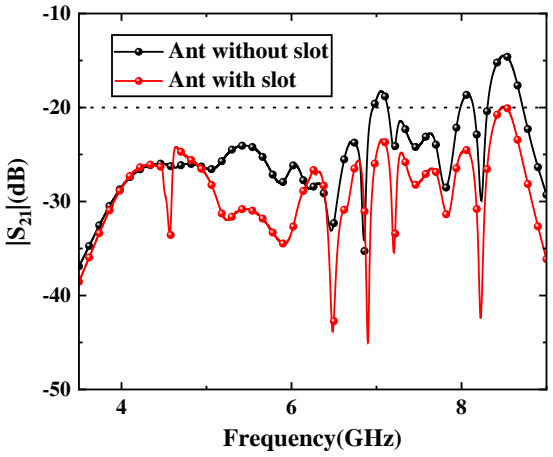

FIGURE 13. S-parameters with and without isolation structures.

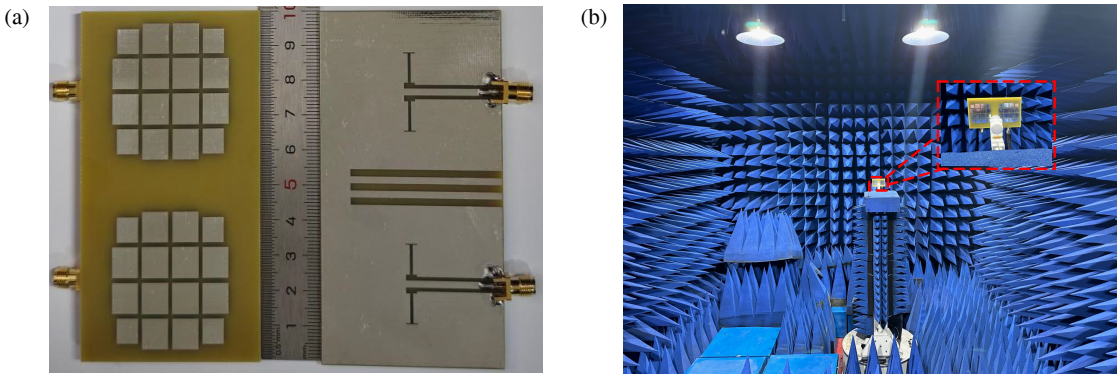

FIGURE 14. Photograph of the prototype in the measurement.

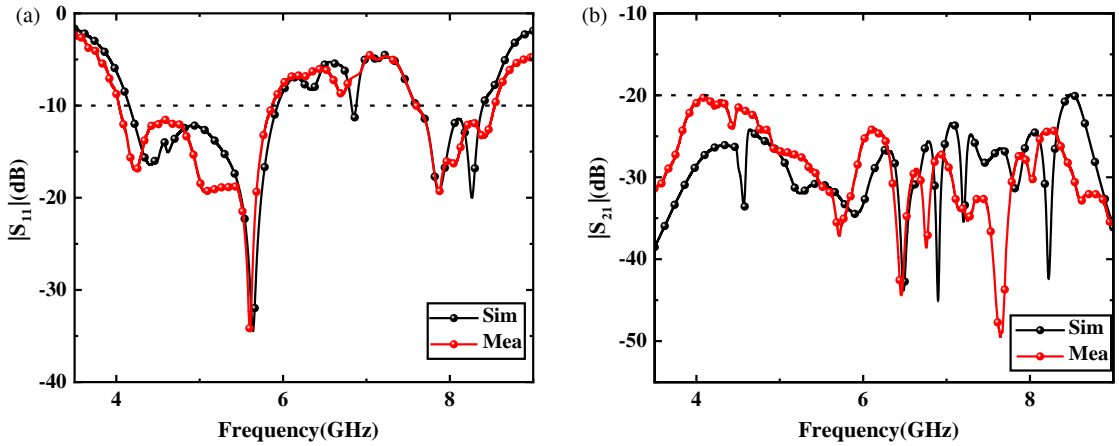

FIGURE 15. Simulated and measured S-parameters.

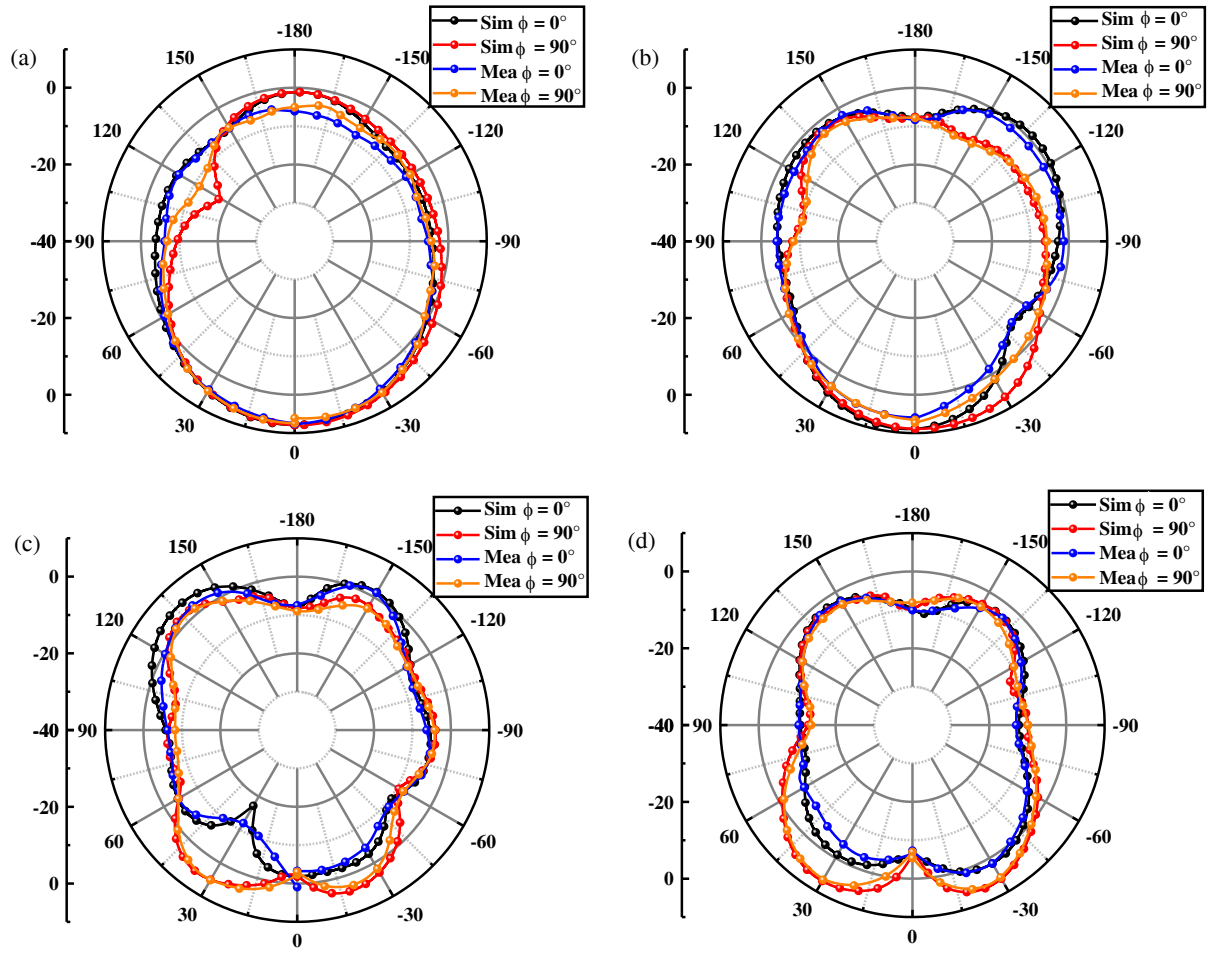

FIGURE 16. Simulated and measured 2D radiation patterns of the proposed MIMO system. (a) 4.42 GHz; (b) 5.66 GHz; (c) 7.86 GHz; (d) 8.24 GHz.

TABLE 1. Antenna performance comparison.

Ref	Bandwidth (%)	ECC	Isolation (dB)	Gain (dB)	Aperture Efficiency (%)	Size
[29]	72.93%	0.005	> 15	8.8	61.7%	$0.966\lambda_o \times 0.766\lambda_o \times 0.053\lambda_o$
[30]	2.9%/28.6%	0.007/0.002	> 19.7	9.1	64.7%/62.2%	$1.7\lambda_o \times 1.7\lambda_o \times 0.051\lambda_o$
[31]	10.8%	Not given	> 22	6	33.7%	$1.9\lambda_o \times 1.9\lambda_o \times 0.07\lambda_o$
[32]	13.04%	0.0015	> 22	8	34.7%	$1.47\lambda_o \times 1.47\lambda_o \times 0.45\lambda_o$
[33]	88%	0.01	> 15	3.8	37%	$1\lambda_o \times 1\lambda_o \times 0.035\lambda_o$
[34]	4.78%	0.01	> 20	5.34	40%	$1.64\lambda_o \times 1.64\lambda_o \times 1.64\lambda_o$
[35]	7.69%/5.71%	0.08/0.01	> 25	8.6	Not given	$1.3\lambda_o \times 0.867\lambda_o \times 0.052\lambda_o$
Proposed	36%/10%	0.0009/0.0025	> 22	10.75	72%/36.8%	$1.67\lambda_o \times 1.67\lambda_o \times 0.05\lambda_o$

λ_o is the free-space wavelength at center operating frequency.

wideband antennas (e.g., 8 dB for [32]). The Envelope Correlation Coefficient (ECC) of this antenna reaches the lowest values in both frequency bands (0.0009/0.0025), indicating the extremely low correlation between antenna elements, which can significantly enhances channel capacity and anti-fading capabilities in MIMO systems. Despite its moderate size ($1.67\lambda_o \times 1.67\lambda_o \times 0.05\lambda_o$) among dual-band antennas, the low-profile design (with a height of only $0.05\lambda_o$) achieves compactness without compromising gain and isolation ($>$ 22 dB), meeting deployment requirements across multiple scenarios. In comparison to other designs, this antenna achieves or exceeds the optimal values in Table 1 for the three core indicators: gain, ECC, and isolation, particularly demonstrating significant advantages in dual-band applications. It is suitable for 5G/6G MIMO communication systems with stringent performance requirements.

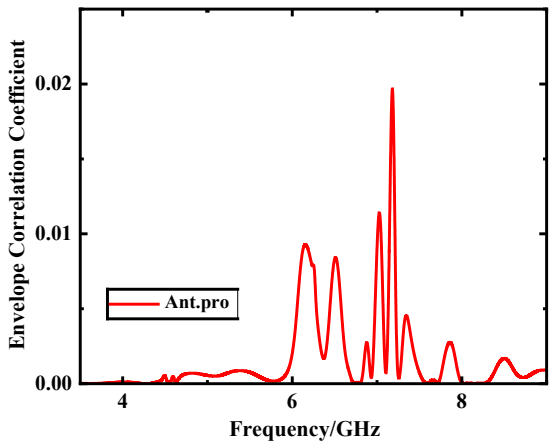

FIGURE 17. Envelope correlation coefficients of MIMO antenna elements.

4. CONCLUSION

This paper proposes a novel single-layer dual-band metasurface-MIMO antenna that employs an H-shaped slot feeding structure to replace the traditional CPW. Combined with a triple-slot decoupling technique on the ground plane, it achieves a dual-band independent design without the need for multilayer stacking or complex matching networks (low-frequency band: 4.13–5.94 GHz, with a relative bandwidth of 36%; high-frequency band: 7.6–8.4 GHz). CMA is utilized to optimize the patch size, effectively exciting a high-order mode (Mode 17), thereby resolving the contradiction between dual-band isolation and structural compactness. Experimental results demonstrate that the antenna achieves isolation below −22 dB within both frequency bands, with an ECC of less than 0.0025 and peak gains reaching 9.56 dB and 10.75 dB, respectively. This verifies its excellent impedance matching, radiation efficiency, and MIMO performance. Compared to existing methods, the planar decoupling strategy avoids metal vias or multilayer structures, significantly reducing manufacturing complexity and cost. This design provides a high-performance antenna solution for high-density 5G base stations, satellite terminals, and IoT devices. It also lays a theoretical foundation for mode decoupling and bandwidth expansion in ultra-compact dual-band MIMO antennas. Future research can further explore the potential applications of this solution in multi-band compatibility and large-scale arrays.

ACKNOWLEDGEMENT

This work was supported in part by the Natural Science Research Project of Anhui Educational Committee under No. 2022AH051583, No. 2022AH052138, and No. 2023AH052650, in part by the Anhui Province Graduate Academic Innovation Project under grant No. 2023xscx074,and in part by the Graduate Innovation Fund of Anhui University of Science and Technology under grant No. 2024cx2063.

REFERENCES

[1] Jensen, M. A. and J. W. Wallace, "A review of antennas and propagation for MIMO wireless communications," *IEEE Transactions on Antennas and Propagation*, Vol. 52, No. 11, 2810–2824, 2004.

[2] Liu, S., S.-S. Qi, W. Wu, and D.-G. Fang, "Single-feed dual-band single/dual-beam U-slot antenna for wireless communication application," *IEEE Transactions on Antennas and Propagation*, Vol. 63, No. 8, 3759–3764, 2015.

[3] Soltani, S., P. Lotfi, and R. D. Murch, "A dual-band multiport MIMO slot antenna for WLAN applications," *IEEE Antennas and Wireless Propagation Letters*, Vol. 16, 529–532, 2016.

[4] Habashi, A., J. Nourinia, and C. Ghobadi, "Mutual coupling reduction between very closely spaced patch antennas using low-profile folded split-ring resonators (fsrrs)," *IEEE Antennas and Wireless Propagation Letters*, Vol. 10, 862–865, 2011.

[5] Yang, X., Y. Liu, Y.-X. Xu, and S.-X. Gong, "Isolation enhancement in patch antenna array with fractal UC-EBG structure and cross slot," *IEEE Antennas and Wireless Propagation Letters*, Vol. 16, 2175–2178, 2017.

[6] Hsieh, C., T. Chiu, and C. Lai, "Compact dual-band slot antenna at the corner of the ground plane," *IEEE Transactions on Antennas and Propagation*, Vol. 57, No. 10, 3423–3426, 2009.

[7] Huang, Y., L. Yang, J. Li, Y. Wang, and G. Wen, "Polarization conversion of metasurface for the application of wide band low-profile circular polarization slot antenna," *Applied Physics Letters*, Vol. 109, No. 5, 054101, 2016.

[8] Zheng, Q., C. Guo, J. Ding, and G. A. E. Vandenbosch, "Dual-band metasurface-based CP low-profile patch antenna with parasitic elements," *IET Microwaves, Antennas & Propagation*, Vol. 13, No. 13, 2360–2364, 2019.

[9] Wang, X., L. Guo, W. Zhou, and Q. Zhang, "A double-layer multimode metasurface antenna using characteristic mode analysis," *IEEE Antennas and Wireless Propagation Letters*, Vol. 23, No. 10, 3237–3241, 2024.

[10] Gao, J. F. and F. H. Lin, "Modeling and analysis of wideband multilayer metasurface antenna array using characteristic-mode analysis," *IEEE Transactions on Antennas and Propagation*, Vol. 71, No. 3, 2832–2836, 2023.

[11] Gao, X., G. Tian, Z. Shou, and S. Li, "A low-profile broadband circularly polarized patch antenna based on characteristic mode analysis," *IEEE Antennas and Wireless Propagation Letters*, Vol. 20, No. 2, 214–218, 2021.

[12] El Yousfi, A., A. Lamkaddem, K. A. Abdalmalak, and D. Segovia-Vargas, "A broadband circularly polarized single-layer metasurface antenna using characteristic-mode analysis," *IEEE Transactions on Antennas and Propagation*, Vol. 71, No. 4, 3114–3122, 2023.

[13] Chen, Q., J. Yang, C. He, L. Hong, D. Zhang, S. Huang, F. Yu, L. Zhang, W. Xiong, and H. Zhang, "Nonuniform metasurface for wideband circularly polarized antenna using characteristic mode analysis," *AEU — International Journal of Electronics and Communications*, Vol. 172, 154978, 2023.

[14] Li, T. and Z. N. Chen, "A dual-band metasurface antenna using characteristic mode analysis," *IEEE Transactions on Antennas and Propagation*, Vol. 66, No. 10, 5620–5624, 2018.

[15] Lin, F. H. and Z. N. Chen, "Resonant metasurface antennas with resonant apertures: Characteristic mode analysis and dual-polarized broadband low-profile design," *IEEE Transactions on Antennas and Propagation*, Vol. 69, No. 6, 3512–3516, 2021.

[16] Chen, Y.-J., T.-W. Liu, and W.-H. Tu, "CPW-fed penta-band slot dipole antenna based on comb-like metal sheets," *IEEE Antennas*

and Wireless Propagation Letters, Vol. 16, 202–205, 2016.

[17] Ghosh, J., D. Mitra, and S. Das, "Mutual coupling reduction of slot antenna array by controlling surface wave propagation," *IEEE Transactions on Antennas and Propagation*, Vol. 67, No. 2, 1352–1357, 2019.

[18] Garg, P. and P. Jain, "Isolation improvement of MIMO antenna using a novel flower shaped metamaterial absorber at 5.5 GHz WiMAX band," *IEEE Transactions on Circuits and Systems II: Express Briefs*, Vol. 67, No. 4, 675–679, 2020.

[19] Adam, I., M. N. M. Yasin, N. Ramli, M. Jusoh, H. A. Rahim, T. B. A. Latef, T. F. T. M. N. Izam, and T. Sabapathy, "Mutual coupling reduction of a wideband circularly polarized microstrip MIMO antenna," *IEEE Access*, Vol. 7, 97 838–97 845, 2019.

[20] Li, M., R. Wang, J. M. Yasir, and L. Jiang, "A miniaturized dual-band dual-polarized band-notched slot antenna array with high isolation for base station applications," *IEEE Transactions on Antennas and Propagation*, Vol. 68, No. 2, 795–804, 2020.

[21] Chen, S.-Y., Y.-C. Chen, and P. Hsu, "CPW-fed aperture-coupled slot dipole antenna for tri-band operation," *IEEE Antennas and Wireless Propagation Letters*, Vol. 7, 535–537, 2008.

[22] Liu, W. E. I., Z. N. Chen, and X. Qing, "Miniature wideband non-uniform metasurface antenna using equivalent circuit model," *IEEE Transactions on Antennas and Propagation*, Vol. 68, No. 7, 5652–5657, 2020.

[23] Ni, C., L. Zhang, and Z. Zhang, "A low profile broadband circularly polarized metasurface antenna based on tri-modal," *IEEE Antennas and Wireless Propagation Letters*, Vol. 23, No. 10, 3267–3271, 2024.

[24] Lin, F. H. and Z. N. Chen, "Low-profile wideband metasurface antennas using characteristic mode analysis," *IEEE Transactions on Antennas and Propagation*, Vol. 65, No. 4, 1706–1713, 2017.

[25] Zhao, C. and C.-F. Wang, "Characteristic mode design of wide band circularly polarized patch antenna consisting of H-shaped unit cells," *IEEE Access*, Vol. 6, 25 292–25 299, 2018.

[26] Peng, H.-L., R. Tao, W.-Y. Yin, and J.-F. Mao, "A novel compact dual-band antenna array with high isolations realized using the neutralization technique," *IEEE Transactions on Antennas and Propagation*, Vol. 61, No. 4, 1956–1962, 2013.

[27] Janaswamy, R., "Effect of element mutual coupling on the capacity of fixed length linear arrays," *IEEE Antennas and Wireless Propagation Letters*, Vol. 1, 157–160, 2002.

[28] Wang, Z., S. Liu, W. Nie, M. Yang, and C. Li, "Broadband eight-element MIMO antenna with high isolation for 5G smartphone applications," *Progress In Electromagnetics Research C*, Vol. 152, 209–219, 2025.

[29] Saxena, G., S. Kumar, S. Chintakindi, A. Al-Tamim, M. H. Abidi, W. A. M. Saif, S. Kansal, R. Jain, S. Singh, A. K. Dohare, *et al.*, "Metasurface instrumented high gain and low RCS X-band circularly polarized MIMO antenna for IoT over satellite application," *IEEE Transactions on Instrumentation and Measurement*, Vol. 72, 1–10, 2023.

[30] Zheng, Q., J. Wang, P. PourMohammadi, and X. Pang, "Dual-band metasurface-based closely packed antennas by controlling surface wave propagation," *IEEE Antennas and Wireless Propagation Letters*, Vol. 23, No. 5, 1633–1637, 2024.

[31] Elahi, M., S. Koziel, and L. Leifsson, "A non-PCM-based 2 x 2 MIMO antenna array with low radar cross-section using characteristic mode analysis," *IEEE Access*, Vol. 13, 34 296–34 306, 2025.

[32] Luo, S., Y. Zhang, G. F. Pedersen, and S. Zhang, "Mutual decoupling for massive MIMO antenna arrays by using triple-layer meta-surface," *IEEE Open Journal of Antennas and Propagation*, Vol. 3, 1079–1089, 2022.

[33] Gangwar, D., A. Sharma, B. K. Kanaujia, S. P. Singh, and A. Lay-Ekuakille, "Characterization and performance measurement of low RCS wideband circularly polarized MIMO antenna for microwave sensing applications," *IEEE Transactions on Instrumentation and Measurement*, Vol. 69, No. 6, 3847–3854, 2020.

[34] Pandit, S., A. Mohan, and P. Ray, "Low-RCS low-profile four-element MIMO antenna using polarization conversion metasurface," *IEEE Antennas and Wireless Propagation Letters*, Vol. 19, No. 12, 2102–2106, 2020.

[35] Liu, F., J. Guo, L. Zhao, G.-L. Huang, Y. Li, and Y. Yin, "Dual-band metasurface-based decoupling method for two closely packed dual-band antennas," *IEEE Transactions on Antennas and Propagation*, Vol. 68, No. 1, 552–557, 2020.